Porphyrin-Sensitized Solar Cells with Cobalt (II/III)–Based Redox Electrolyte Exceed 12 Percent Efficiency

Aswani Yella, *et al.*

Science **334**, 629 (2011);
DOI: 10.1126/science.1209688

Porphyrin-Sensitized Solar Cells with Cobalt (II/III)–Based Redox Electrolyte Exceed 12 Percent Efficiency

Aswani Yella,[1] Hsuan-Wei Lee,[2] Hoi Nok Tsao,[1] Chenyi Yi,[1] Aravind Kumar Chandiran,[1] Md.Khaja Nazeeruddin,[1] Eric Wei-Guang Diau,[3]* Chen-Yu Yeh,[2]* Shaik M Zakeeruddin,[1]* Michael Grätzel[1]*

The iodide/triiodide redox shuttle has limited the efficiencies accessible in dye-sensitized solar cells. Here, we report mesoscopic solar cells that incorporate a $Co^{(II/III)}$tris(bipyridyl)–based redox electrolyte in conjunction with a custom synthesized donor-π-bridge-acceptor zinc porphyrin dye as sensitizer (designated **YD2-*o*-C8**). The specific molecular design of **YD2-*o*-C8** greatly retards the rate of interfacial back electron transfer from the conduction band of the nanocrystalline titanium dioxide film to the oxidized cobalt mediator, which enables attainment of strikingly high photovoltages approaching 1 volt. Because the **YD2-*o*-C8** porphyrin harvests sunlight across the visible spectrum, large photocurrents are generated. Cosensitization of **YD2-*o*-C8** with another organic dye further enhances the performance of the device, leading to a measured power conversion efficiency of 12.3% under simulated air mass 1.5 global sunlight.

Dye-sensitized solar cells (DSCs) have recently received great attention because of their ease of fabrication and cost-effectiveness compared with silicon (Si)–based photovoltaic devices (*1*). So far, the best conversion efficiencies have been obtained with ruthenium-based dyes used together with the iodide/triiodide redox couple (*2*–*10*). Upon optical excitation, the dye injects an electron into the conduction band of a nanocrystalline film of a wide band gap oxide, such as titanium dioxide (TiO_2), and is subsequently regenerated back to the ground state by electron donation from a redox couple present in the electrolyte. In this fashion, the DSC achieves the separation of light harvesting and charge generation from charge carrier transport, whereas all other known photovoltaic devices, including Si cells, perform both operations simultaneously. This imposes stringent demands on the puritiy of the semiconductor—99.9999% for solar grade Si—resulting in high material cost and long energy payback times. The separation of the functions of light absorption and carrier transport achieved by the DSC has many advantages, key points being a large choice of light absorber and charge transport materials, which can be applied by simple screen printing methods and do not have to undergo costly purification or doping treatments. Although the DSC already outperforms its competitors in ambient light and indoor conditions, its validated solar-to-electric power-conversion efficiency (PCE) under standard air mass 1.5 (AM 1.5) reporting conditions (1000 W/m^2 solar light intensity and 298 K) of 11.1% (*2*) is still a factor of 2 below that of Si solar cells. (The air mass number expresses the ratio of the path length of the solar light in the atmosphere over that corresponding to vertical position of the sun. At air mass 1.5, the sun is at an angle of 48.19° with regard to the vertical axes).

Because of an excessive loss of voltage during the dye-regeneration reaction, the use of the iodide/triiodide electrolyte as a redox shuttle limits the attainable open-circuit potential, V_{oc}, to 0.7 to 0.8 V and is thus a drawback of current DSC embodiments. This has prevented substantial gains in PCE over the last 5 years (*11*). To further improve the PCE, development of redox mediators exhibiting higher reduction potentials than that of I_3^- is warranted; $Co^{(II/III)}$tris(bipyridyl) complexes do have this property. However, such one-electron, outer-sphere redox couples often yield shorter electron lifetimes when used in the DSC. This faster interfacial charge recombination, when compared with iodide/triiodide–based redox electrolytes (*12*–*18*), lowers the photovoltage and reduces the efficiency of charge collection, decreasing the short circuit photocurrent density (J_{sc}) and hence the PCE (*19*–*21*). Recent evidence suggests that the introduction of long-chain alkyloxy groups in the dye structure may retard the unwanted charge recombination process (*22*). Donor-π-bridge-acceptor (D-π-A) sensitizers, endowed with such groups, recently reached V_{oc} values exceeding 0.8 V when used with $Co^{(II/III)}$tris(bipyridyl) redox electrolytes. However, the PCEs of these devices remained in the 6.7 to 9.6% range because of their insufficient solar light harvesting, resulting in low photocurrents (*22*–*24*). This rationale has inspired us to synthesize a D-π-A zinc (Zn) porphyrin dye, designated **YD2-*o*-C8,** which absorbs light over the whole visible range and is endowed with long-chain alkoxy groups so as to impair interfacial back electron transfer reaction. When used in conjuntion with cobalt polypyridyl–based redox electrolytes, **YD2-*o*-C8** achieves conversion efficiencies exceeding those obtained with today's best ruthenium sensitizers.

Inspired by the important role that porphyrins play in natural photosynthesis, researchers have tested numerous derivatives of this substrate class as sensitizers for DSCs, but conversion efficiencies obtained so far have largely remained below 8% (*25*–*33*). An exception is the class of D-π-A porphyrin dyes, such as **YD2,** which has reached a PCE of 11% when used with iodide/triiodide redox electrolyte (*34*). A diarylamine group attached to the porphyrin ring acts as an electron donor, and an ethynylbenzoic acid moiety serves as an acceptor, anchoring the dye to the titania surface. The unique feature of these sensitizers is that the porphyrin chromophore itself constitutes the π-bridge of the D-π-A structure (*35*–*40*). The judiciously tailored variant of **YD2** that we report here,**YD2-*o*-C8** (Fig. 1), incorporates two octyloxy groups in the *ortho* positions of each *meso*-phenyl ring, producing a striking

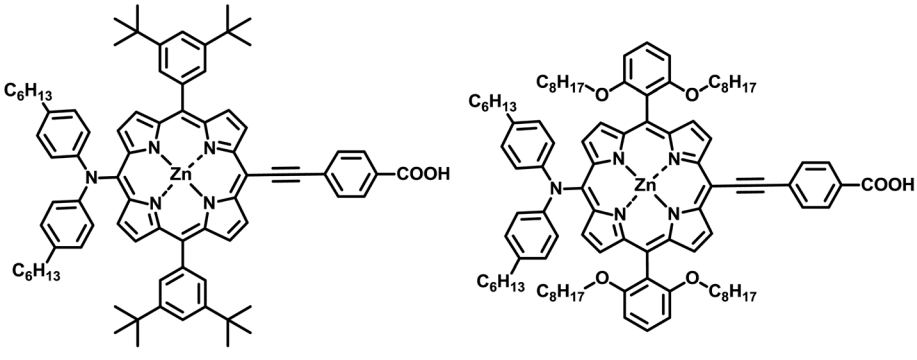

Fig. 1. The molecular structures of the (**left**) **YD2** and (**right**) **YD2-*o*-C8** porphyrin dyes.

[1]Laboratory for Photonics and Interfaces, Institute of Chemical Sciences and Engineering, École Polytechnique Fédérale de Lausanne, Lausanne-1015, Switzerland. [2]Department of Chemistry and Center of Nanoscience and Nanotechnology, National Chung Hsing University, Taichung, Taiwan 402, ROC. [3]Department of Applied Chemistry and Institute of Molecular Science, National Chiao Tung University, Hsinchu, Taiwan 300, ROC.

*To whom correspondence should be addressed. E-mail: michael.graetzel@epfl.ch (M.G.); shaik.zakeer@epfl.ch (S.M.Z.); diau@mail.nctu.edu.tw (E.W.-G.D); cyyeh@dragon.nchu.edu.tw (C.-Y.Y.)

amelioration of the photo-induced charge separation in DSCs using $Co^{(II/III)}$tris(bipyridyl)–based redox electrolyte. High PCE values reaching 11.9% have been achieved with this molecular photovoltaic system, which produces a V_{oc} of 965 mV, a J_{sc} of 17.3 mA/cm^2, and a fill factor (FF) of 0.71 under standard AM 1.5 sunlight at 995 W/m^2 intensity. The cosensitization of **YD2-*o*-C8** with the previously prepared organic D-π-A dye, coded **Y123**, yielded an efficiency of 12.3% when used in conjunction with the $Co^{(II/III)}$tris(bipyridyl)–based redox electrolyte. The PCE even exceeds 13% under AM 1.5 solar light of 500 Wm^{-2} intensity.

Molecular properties and photovoltaic performance. The detailed synthetic procedure for preparing the **YD2-*o*-C8** porphyrin is described in the supporting online material (SOM). Absorption spectra of these two porphyrin dyes measured in tetrahydrofuran (THF) solvent are shown in fig. S1, and table S1 lists the corresponding spectral properties. Both porphyrins exhibit maxima in the 400 to 500 nm and 550 to 750 nm ranges, corresponding to the Soret and Q bands, respectively, with similar molar absorption coefficients. Nevertheless, the Soret band of **YD2-*o*-C8** is slightly red-shifted, and its Q band is narrower as compared with the **YD2** spectrum. This is ascribed to the electronic effect of the two electron-donating dioctyloxy substituents introduced in *ortho*-position of the *meso*-phenyl ring. The emission behavior for the two sensitizers matches their absorption spectra, the fluorescence maximum of **YD2-o-C8** being blue-shifted by 13 nm relative to that of **YD2**. The oxidation potentials of the two dyes were determined by means of cyclic voltammetry (CV). **YD2-*o*-C8** shows two oxidation waves at half-wave potential ($E_{1/2}$) = +0.82 and +1.37 V versus normal hydrogen electrode (NHE) (fig. S2). These values are lower than the corresponding potentials of **YD2** (table S1) because of the electron-donating substituents on the *meso*-phenyl rings. The 190-mV negative shift of the reduction potential of **YD2-*o*-C8** corresponds to a lifting of the lowest unoccupied molecular orbital (LUMO) level and is a manifestation of the same effect.

To gain further insight into the electron density distribution within the frontier and other close-lying orbitals, we performed quantum chemical calculations on the **YD2-*o*-C8** porphyrin using density functional theory (DFT) at the B3LYP/6-31G(d) level [Spartan 08 package (Wavefunction, Irvine, CA)] and compared them with the calculated electronic structure of the **YD2** dye (fig. S3). In the ground state, the electron density of **YD2** for the highest occupied molecular orbital (HOMO) and HOMO-1 is shared by the diphenylamine donor moiety and the π-system of the porphyrin ring. Introduction of the strongly electron-donating group (octyloxy) at the *ortho*-positions of phenyl rings, attached at the *meso*-positions of porphyrin core in **YD2-*o*-C8**, increases the electronic density on the porphyrin π-system over *tert*-butyl groups present at the HOMO and HOMO-1 level of the **YD2** dye. Thus, for **YD2-*o*-C8** there is a considerable electronic coupling between the alkoxy groups and the porphyrin core, lifting the LUMO level higher than that of the **YD2** dye. The predicted effect is an increase of the HOMO-LUMO gap of **YD2-*o*-C8** compared with **YD2** dye, which is in good agreement with the experimental observations.

Photovoltaic experiments were conducted with an electrolyte by using the $Co^{(II/III)}$tris(bipyridyl) tetracyanoborate complexes as redox couple. The optimized electrolyte composition, designated AY1, consists of 0.165 M $[Co^{II}(bpy)_3](B(CN)_4)_2$, 0.045 M $[Co^{III}(bpy)_3](B(CN)_4)_3$ along with 0.8 M *tert*-butyl pyridine (TBP), and 0.1 M $LiClO_4$ in acetonitrile as a solvent. Details on the optimization of the concentration for the electrolyte components are presented in fig. S4. Using the Nernst equation and standard potential (E^o) = 0.57 V versus NHE for the experimentally determined (*23*) standard potential of the $Co^{(II/III)}$tris(bipyridyl) tetracyanoborate couple, the oxidation potential for this electrolyte is derived as 0.535 V versus NHE.

Performance in a $Co^{(II/III)}$tris(bipyridyl)–mediated solar cell. Photocurrent density versus voltage (*J-V*) is shown in Fig. 2A; the curves were measured under standard photovoltaic reporting conditions (AM 1.5 global sunlight at 1000 W/m^2 and a temperature of 298 K) for cells with **YD2-*o*-C8** or **YD2** sensitizers used in conjunction with the AY1 electrolyte. **YD2-*o*-C8** gives a PCE of 11.9% compared with only 8.4% for the reference dye **YD2.** The key observation here is that a subtle modification of the porphyrin structure induces strikingly large J_{sc} and V_{oc} improvements. This performance advantage is maintained over a large range of light intensities, ranging from 10% to full solar intensity (Table 1).

The incident monochromatic photon-to–electric current conversion efficiency (IPCE) as a function of wavelength and *J-V* curves for the same **YD2** and **YD2-*o*-C8** devices is presented in Fig. 2. **YD2-*o*-C8** shows impressively high IPCE values over the whole visible wavelength range, exceeding 80% from 450 nm up to 680 nm, except for a narrow dip in the spectrum around 530 nm. The spectral response of the photocurrent obtained with the **YD2** cell shows similar features, with peaks at around 460 and 650 nm. However, the absolute IPCE values are 20 to 30% lower for **YD2** as compared with **YD2-*o*-C8**, despite its higher molar extinction coefficient, which is in keeping with the lower short-circuit photocurrent densities observed for **YD2** in Fig. 2A. The J_{sc} values obtained from calculating the overlap integral of the IPCE spectrum with the standard AM 1.5 global spectral solar photon flux were 17.3 and 14.9 mA/cm^2 for **YD2-*o*-C8** and **YD2**, respectively. These figures agree within 2% with the measured J_{sc}, showing that any spectral mismatch between the simulated and true AM 1.5 solar emission is very small with the solar simulator used in our experiments.

The four factors determining the IPCE are the light-harvesting efficiency (LHE), the quantum yield of electron injection from the excited sensitizer into the TiO_2 conduction band (Φ_{inj}), the efficiency for dye regeneration (η_{reg}), and the collection efficiency of the photo-generated charge carriers (η_{coll}):

$$IPCE = LHE\ \Phi_{inj}\ \eta_{reg}\ \eta_{coll} \quad (1)$$

The charge carrier collection efficiency is determined in turn by the time constant for transport (τ_{trans}) and recombination (τ_{rec}) of the conduction

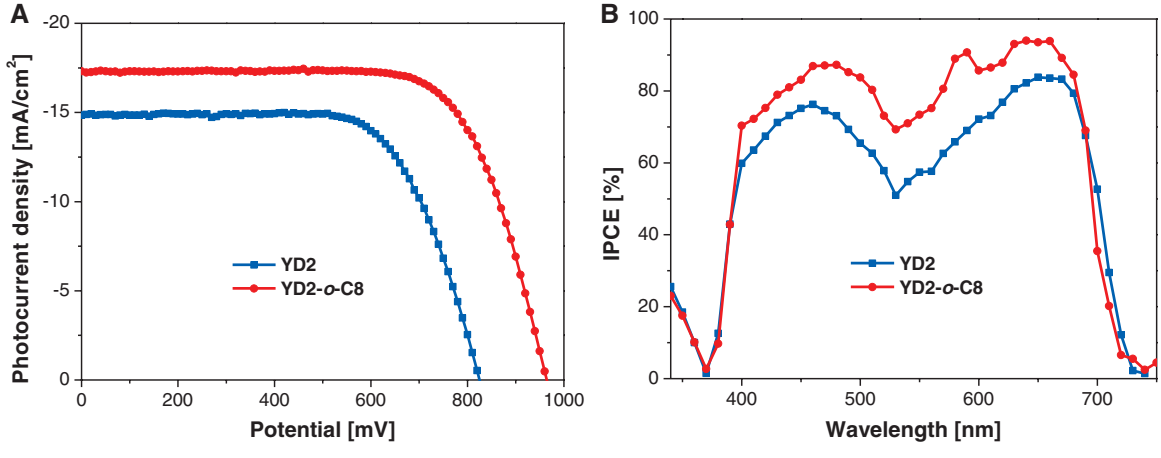

Fig. 2. (**A**) Comparison of the *J-V* curves of **YD2-*o*-C8**– and **YD2**-sensitized solar cells under full AM 1.5 solar intensity. (**B**) Incident photon-to–electric current conversion efficiencies as a function of wavelength for the two dyes (**YD2-*o*-C8**, red; **YD2**, blue). The TiO_2 film thickness is a 5-μm transparent layer and on top a 5-μm scattering layer.

band electrons injected into the nanocrystalline TiO_2 film:

$$\eta_{coll} = 1/(1 + \tau_{trans}/\tau_{rec}) \quad (2)$$

We separately examined the four efficiency parameters of Eq. 1 in order to elucidate the reasons for the much higher IPCE values obtained with **YD2-*o*-C8** as compared with the **YD2** porphyrin. The LHE of a 6-μm-thick transparent TiO_2 film loaded with a monolayer of the sensitizer is shown in Fig. 3. The LHE for the two porphyrins is very similar, the Q-band for **YD2-*o*-C8** being slightly shifted to the blue with respect to that of **YD2**, which matches the behavior of the absorption spectra. The LHE reaches close to 100% near the Soret and Q bands, even for the 6-μm-thick transparent TiO_2 film. The spectral domain where all the photons are captured by the dye-sensitized mesoscopic TiO_2 film is further broadened for the 10-μm-thick double layer used in Fig. 2 because of the increase of the optical path length by light scattering from the top particle layer. This rules out that a change in the LHE causes the difference in the IPCE and J_{sc} values for the two porphyrins (*34*).

Table 1. Detailed photovoltaic parameters of the devices made with the dyes **YD2** and **YD2-*o*-C8** and cobalt-based AY1 electrolyte at different light intensities. P_{in}, incident intensity of AM1.5 solar light.

Dye	Electrolyte	P_{in} (mW/cm^2)	J_{sc} (mA/cm^2)	V_{oc} (mV)	FF	PCE (%)
YD2	AY1	9.4	1.5	745	0.82	9.5
		51.3	8.0	805	0.76	9.5
		99.8	14.9	825	0.69	8.4
YD2-*o*-C8	AY1	9.4	1.7	875	0.77	12.5
		51.2	9.3	940	0.74	12.7
		99.5	17.3	965	0.71	11.9

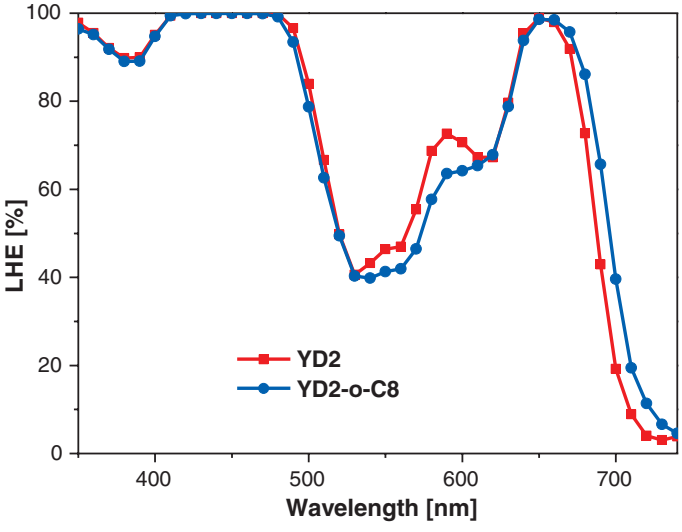

Fig. 3. LHE as a function of wavelength for the **YD2** and **YD2-o-C8** porphyrins adsorbed at the surface of a 6-μm-thick nanocrystalline TiO_2 film.

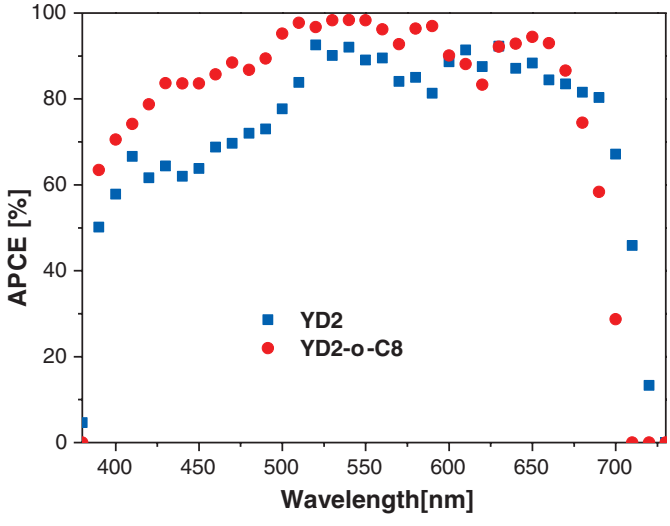

Fig. 4. APCE as a function of wavelength for the **YD2** and **YD2-*o*-C8** porphyrin adsorbed at the surface of a 6-μm-thick nanocrystalline TiO_2 film in contact with $Co^{(II/III)}$tris(bipyridyl)–based electrolyte.

Dividing the IPCE by the LHE gives the absorbed photon-to–electric current generation efficiency (APCE), presenting the true quantum yield for electric current generation from light. The APCE values in the wavelength range from 420 to 700 nm are between 80 and 100%, and 60 to 90% for **YD2-o-C8** and **YD2**, respectively (Fig. 4). This indicates that the electron injection, dye regeneration, or charge carrier collection is less efficient for the latter than for the former sensitizer when used in conjunction with the $Co^{(II/III)}$tris(bipyridyl) tetracyanoborate complexes as redox couple.

We performed time-resolved luminescence experiments to unravel any differences in the dynamics of photo-induced electron injection between the two porphyrins. In fig. S5, we compare emission data in THF solution and for **YD2-o-C8**– or **YD2**-covered nanocrystalline TiO_2 films in contact with the same $Co^{(II/III)}$tris(bipyridyl)–based redox electrolyte used in the photovoltaic experiments. In solution, the fluorescence lifetimes for **YD2-*o*-C8** and **YD2** are 1.5 and 1.2 ns, respectively, whereas the emission for both sensitizers is strongly quenched in contact with TiO_2. Data fitting, including reconvolution of the emission signal over the ~1 ns excitation pulse length, indicates that the lifetime of the excited singlet state of the two porphyrins in the adsorbed state is at most 100 ps. These experiments do not reveal any significant difference in the fluorescence kinetics of the two porphyrins. There is also little doubt that the very rapid quenching of luminescence leads in both cases to near-quantitative charge injection from their excited singlet state to the conduction band of the TiO_2 nanocrystals, as implied by the very high APCE values observed for **YD2-*o*-C8** in Fig. 4 and the near-unity IPCE values for **YD2** obtained with iodide/triiodide–based redox electrolytes.

The data obtained from intensity-modulated photo-induced absorption (PIA) measurements (*41*) shown in the top row of fig. S6 confirm the occurrence of oxidative quenching after light excitation of the two porphyrins adsorbed on the nanocrystalline TiO_2 film. The absorption peaks at 550, 800, and 1400 nm reveal the formation of porphyrin radical cations by electron injection from the excited state in the conduction band of the titania. The two PIA spectra in the lower row show that these features disappear completely in the presence of the $Co^{(II/III)}$tris(bipyridyl) electrolyte, indicating complete regeneration of the **YD2** or **YD2-*o*-C8** porphyrins through electron donation from the Co(II) form of the redox couple.

Because the LHE as well as the quantum yield for electron injection and regeneration are very high for both dyes, we reasoned that the lower IPCE values for **YD2** as compared with **YD2-*o*-C8** reflect differences in the efficiency for carrier collection between the two porphyrin sensitizers.

Inhibition of back electron transfer. We used transient photocurrent and photovoltage decay measurements to compare the rates of interfacial

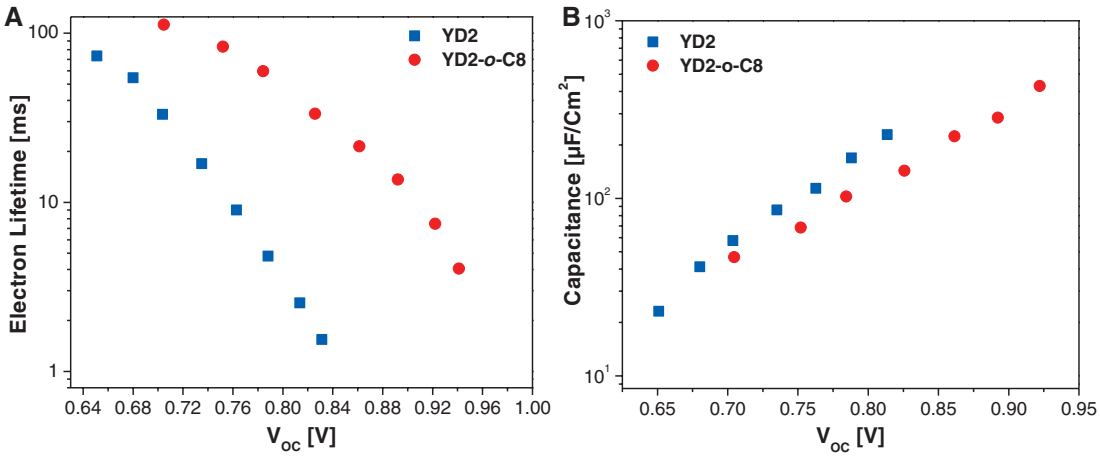

Fig. 5. Electron (**A**) lifetime and (**B**) capacitance determined with photocurrent and photovoltage decay measurements of devices with **YD2** and **YD2-*o*-C8** dyes.

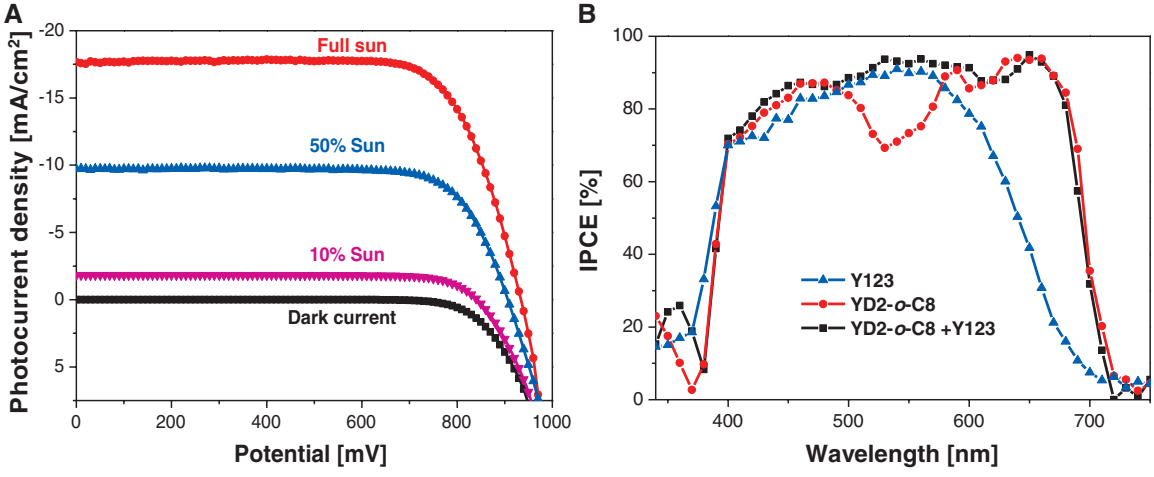

Fig. 6. (**A**) *J-V* characteristics of a **YD2-*o*-C8/Y123** cosensitized DSC, measured under standard AM 1.5 global sunlight under various light intensities. The molar **YD2-*o*-C8/Y123** ratio in the dye solution was 7. (**B**) Spectral response of the IPCE for **YD2-*o*-C8** (red dots), **Y123** (blue triangles), and **YD2-*o*-C8/Y123** cosensitized nanocrystalline TiO_2 films (black squares)

recombination of electrons from the TiO_2 conduction band to Co^{III}tris(bipyridyl) (*42*, *43*). The electron lifetime as a function of V_{oc} for **YD2** and **YD2-*o*-C8** is plotted in Fig. 5A. The V_{oc} was adjusted by varying the intensity of the bias light impinging on the cell. The electron lifetime is 2 to 10 times longer for **YD2-*o*-C8**– than for **YD2**-sensitized TiO_2 films, the difference becoming larger as the V_{oc} increases. One plausible explanation of this observation is that at open circuit, electrons in the conduction band of TiO_2 (e^-_{TiO2}) reacts faster with Co^{III}tris(bipyridyl) for films loaded with the latter than with the former dye.

It appears that the specific molecular structure of **YD2-*o*-C8**—in particular, the presence of the four octyloxy groups—reduces the recombination rate, most likely by inhibiting the access by Co^{III}tris(bipyridyl) to the TiO_2 surface. The distance dependence of the back reaction is in accordance with the semiclassical electron transfer theory (*44*, *45*).

The lower rate of electron recapture by Co^{III}tris(bipyridyl) for **YD2-*o*-C8**–sensitized nanocrystalline TiO_2 films allows very high open-circuit voltages to be realized, with this sensitizer reaching a value of 965 mV in full sunlight without sacrificing short circuit photocurrent or fill factor. The voltage advantage of **YD2-*o*-C8** over **YD2** is maintained at lower light levels, down to 3 W/m^2 solar intensity (fig. S7). The $Co^{II/III}$tris(bipyridyl) electrolyte yields slopes of 90 mV/decade and 80 mV/decade, corresponding to ideality factors $m = 1.52$ and 1.35 in the diode equation for **YD2-*o*-C8** and **YD2** dyes, respectively. This suggests that surface-trapping states participate in the back-electron transfer reaction, which is similar to the findings by Hagfeldt and co-workers (*22*).

It may be argued that the higher V_{oc} observed with **YD2-*o*-C8** with respect to **YD2** arises from a larger dipole moment of the former as compared with the latter sensitizer in the adsorbed state, causing an upward shift of the conduction band of TiO_2. This would displace the trap-state distribution function toward higher energies, rendering the density of occupied states (DOS) at a given forward bias voltage lower for **YD2-*o*-C8** than for **YD2.** To check this possibility, the DOS of the films loaded with sensitizer was determined from transient photocurrent decay measurements (*42*, *43*). The chemical capacitance C_μ for the **YD2-*o*-C8**– and **YD2**-sensitized films as a function of V_{oc} are compared in Fig. 5B. C_μ is directly proportional to the DOS: $C_\mu = q(e)$ DOS, where $q(e)$ is the charge of one electron. The C_μ values are very similar for the two sensitizers, with small differences being noted only at $V_{oc} > 0.8$ V. This rules out any substantial contribution of a conduction band shift to the observed decrease in the back-electron transfer rate.

Using **YD2-*o*-C8** as a sensitizer, we compared the photovoltaic performance of $Co^{II/III}$tris(bipyridyl) with that of a I^-/I_3^-–based redox electrolyte using again a (5+5) μm double-layer TiO_2 film. The concentrations of I^- and I_3^- in this electrolyte, designated AY2, were identical to those of the Co^{2+} and Co^{3+} tris(bipyridyl) in AY1; the other additives, such as TBP and $LiClO_4$, were also maintained at the same levels, as was the acetonitrile solvent. The results presented in table S2 and fig. S8 show that the photovoltaic performance of devices using the $Co^{II/III}$tris(bipyridyl) electrolyte is far superior to that of the I^-/I_3^-–based devices. The V_{oc} and J_{sc} values increase by 193 mV and 2.3 mA/cm^2, respectively, producing a 58% gain of the PCE from 7.6 to 11.9%. To evaluate the photovoltaic performance of the newly designed **YD2-*o*-C8** dye under conditions that are optimal for I^-/I_3^-–based DSCs, a thicker double-layer TiO_2 film of (12+5) μm was applied along with the Z959 standard volatile electrolyte [1.0 M 1,3-dimethylimidazolium iodide (DMII), 0.03 M iodine, 0.1 M guanidinium thiocyanate, and 0.5 M *tert*-butylpyridine in a mixture of valeronitrile/acetonitrile (15:85 v/v)]. Under these conditions, the PCE reached 9.4% (detailed photovoltaic parameters are in table S2). These results

Table 2. Detailed photovoltaic parameters of the devices made with AY1 electrolyte and **YD2-*o*-C8** dye cosensitized with **Y123** dye at different light intensities.

P_{in} (mW/cm^2)	J_{sc} (mA/cm^2)	V_{oc} (mV)	FF	η (%)
9.4	1.83	840	0.79	13.0
50.8	9.72	910	0.76	13.1
99.5	17.66	935	0.74	12.3

confirm that for **YD2-*o*-C8**, the $Co^{II/III}$tris(bipyridyl) complex outperforms the I^-/I_3^-–based redox electrolyte, even under optimal conditions for the latter.

Despite having excellent light-harvesting properties, the **YD2-*o*-C8** dye lacks absorption in the 480 to 630 nm range, as evidenced by the IPCE spectra in Figs. 2B and 6B. The dip in the green spectral region reduces the J_{SC} and hence the PCE. To avoid this loss, we used a cosensitizer coded **Y123** (a D-π-A dye whose structure is shown in fig. S9) that possesses a complementary absorption spectrum to **YD2-*o*-C8**. **Y123** exhibits an absorption maximum at 532 nm in THF with an extinction coefficient of 53,000 M^{-1} cm^{-1} (*23*). This coincides with the minimum in the spectral IPCE response of the **YD2-*o*-C8** dye, the absorption maximum of which is at 644 nm (ε = 31,200 M^{-1} cm^{-1}).

Enhanced performance from adding a cosensitizer. The cosensitized films achieved better photovoltaic performance than that of solar cells using a single dye. The photocurrent *J-V* curves measured at three different light intensities, using the AY1 redox electrolyte, are shown in Fig. 6A. The photovoltaic performance parameters are listed in Table 2. Increased short-circuit current density and FF are observed for the cosensitized films compared with **YD2-*o*-C8** alone. The cumulative increases of J_{sc} and FF give rise to an efficiency of 12.3% at AM 1.5 global full sun using the $Co^{II/III}$tris(bipyridyl)–based redox electrolyte. The PCE reached an even higher value of 13.1% at 509 W/m^2 solar intensity (50.9% sun). These results were independently verified by repeating the photovoltaic characterization of the cells in the Photovoltaic Laboratory at the Institute of Micro Technique (IMT), Neuchâtel, Switzerland. The Wacom high-precision class AAA solar simulator system available at the IMT Photovoltaic Laboratory very closely mimics the solar spectrum in the absorption range of the cosensitized solar cells in the range of 350 to 750 nm. This avoids any substantial spectral mismatch between the simulated and true AM 1.5 solar light source. Results shown in fig. S10 and table S3 fully confirm the PCE measurements carried out in our own laboratory.

The IPCE spectra of devices made with the individual and combined dyes are shown in Fig. 6B. The J_{sc} value obtained from integrating the product of the IPCE spectrum with the AM 1.5 global spectral solar photon flux was 18.3 mA/cm^2. This value is greater than the measured J_{sc} value (17.6 mA/cm^2) at full sunlight. The difference can be attributed to mass transport limitations at full sunlight, which limit the photocurrent. This effect is corroborated by the photocurrent transient measurements by using an on/off modulation of the incident light (*46*). The data reported in fig. S11 show a spike in the photocurrent, which reaches a lower stationary value after a few seconds of illumination time. Our goal is to eliminate this small J_{sc} loss so as to attain a strictly linear response of the photocurrent up to full solar intensity. Such linear behavior already can be achieved by reducing the porphyrin content in the **YD2-*o*-C8/Y123**–containing staining solution from 7:1 to 4:1, as shown in table S4. This indicates that the mass transport limitation is also partly caused by the bulky nature of the **YD2-*o*-C8** dye. Because the increase in **Y123** content in the dye mixture also reduces the V_{oc} value, the linear photocurrent response does not contribute to the PCE at full sunlight.

The **YD2-*o*-C8/Y123** cosensitized nanocrystalline TiO_2 film exhibit an impressive panchromatic photocurrent response over the whole visible range, achieving incident photon-to-electron conversion efficiencies of >90% in a large wavelength domain below 700 nm. Although the cosensitization increases the J_{sc}, the V_{oc} decreases by about 30 mV with respect to films sensitized by **YD2-*o*-C8** alone. Transient photo-voltage decay measurements giving access to the electron lifetime were used to examine the reason for this decrease. The plots of electron lifetime versus open-circuit potential in fig. S12 show that the incorporation of **Y123** reduced the lifetime of the photo-generated electrons in the TiO_2 conduction band compared with **YD2-*o*-C8** alone.

Continued exposure of **YD2-*o*-C8**–sensitized solar cells for 220 hours to full sunlight at 30°C showed only a 10 to 15% decrease of the overall efficiency over this extended light-soaking period. This shows that the photosystem is robust and that the small decline is probably caused by losses of the volatile acetonitrile solvent.

The present results provide a fertile base for further investigation, which will focus on achieving linear response of the photocurrent to full sunlight, enabling PCE values above 13% to be reached under standard reporting conditions. Further challenges to be tackled are the use replacement of the volatile electrolyte by nonvolatile ionic liquid-based systems, as well as solid-state hole conductors. Last, new anchoring groups will be introduced in the porphyrin in order to avoid any desorption on long-term heat and light exposure, along with functional groups increasing the near-infrared response of the sensitizer.

References and Notes

1. B. O'Regan, M. Grätzel, *Nature* **353**, 737 (1991).
2. Y. Chiba *et al.*, *Jpn. J. Appl. Phys.* **45**, L638 (2006).
3. C.-Y. Chen *et al.*, *ACS Nano* **3**, 3103 (2009).
4. W. Zeng *et al.*, *Chem. Mater.* **22**, 1915 (2010).
5. Q. Yu *et al.*, *ACS Nano* **4**, 6032 (2010).
6. J. M. Kroon *et al.*, *Prog. Photovolt. Res. Appl.* **15**, 1 (2007).
7. M. K. Nazeeruddin *et al.*, *J. Am. Chem. Soc.* **127**, 16835 (2005).
8. Y. Chiba, A. Islam, R. Komiya, N. Koide, L. Y. Han, *Appl. Phys. Lett.* **88**, 223505 (2006).
9. Z. S. Wang, M. Yanagida, K. Sayama, H. Sugihara, *Chem. Mater.* **18**, 2912 (2006).
10. M. D. Wei *et al.*, *J. Mater. Chem.* **16**, 1287 (2006).
11. G. Boschloo, A. Hagfeldt, *Acc. Chem. Res.* **42**, 1819 (2009).
12. M. Wang, N. Chamberland, L. Breau, J.-E. Moser, R. H.-Baker, B. Marsan, S. M. Zakeeruddin, M. Grätzel, *Nat. Chem.* **2**, 385 (2010).
13. D. Li *et al.*, *Adv. Funct. Mater.* **20**, 3358 (2010).
14. T. Daeneke *et al.*, *Nat. Chem.* **3**, 211 (2011).
15. Y. Bai *et al.*, *Chem. Commun. (Camb.)* **47**, 4376 (2011).
16. B. A. Gregg, F. Pichot, S. Ferrere, C. L. Fields, *J. Phys. Chem. B* **105**, 1422 (2001).
17. S. Hattori, Y. Wada, S. Yanagida, S. Fukuzumi, *J. Am. Chem. Soc.* **127**, 9648 (2005).
18. Z. Zhang, P. Chen, T. N. Murakami, S. M. Zakeeruddin, M. Grätzel, *Adv. Funct. Mater.* **18**, 341 (2008).
19. H. Nusbaumer, S. M. Zakeeruddin, J. E. Moser, M. Grätzel, *Chemistry* **9**, 3756 (2003).
20. S. A. Sapp, C. M. Elliott, C. Contado, S. Caramori, C. A. Bignozzi, *J. Am. Chem. Soc.* **124**, 11215 (2002).
21. H. Nusbaumer, J. E. Moser, S. M. Zakeeruddin, M. K. Nazeeruddin, M. Gratzel, *J. Phys. Chem. B* **105**, 10461 (2001).
22. S. M. Feldt *et al.*, *J. Am. Chem. Soc.* **132**, 16714 (2010).
23. H. N. Tsao *et al.*, *ChemSusChem* **4**, 591 (2011).
24. Z. Difei *et al.*, *Environ. Sci.* **4**, 2030 (2011).
25. J. N. Clifford, G. Yahioglu, L. R. Milgrom, J. R. Durrant, *Chem. Commun. (Camb.)* **12**, 1260 (2002).
26. T. Hasobe *et al.*, *J. Am. Chem. Soc.* **127**, 1216 (2005).
27. T. Hasobe *et al.*, *J. Phys. Chem. B* **109**, 19 (2005).
28. M. Borgstrçm *et al.*, *J. Phys. Chem. B* **109**, 22928 (2005).
29. C.-W. Lee *et al.*, *Chem. Eur. J.* **15**, 1403 (2009).
30. A. Huijser, T. J. Savenije, A. Kotlewski, S. J. Picken, L. D. A. Siebbeles, *Adv. Mater. (Deerfield Beach Fla.)* **18**, 2234 (2006).
31. O. Hagemann, M. Jørgensen, F. C. Krebs, *J. Org. Chem.* **71**, 5546 (2006).
32. G. M. Hasselman *et al.*, *J. Phys. Chem. B* **110**, 25430 (2006).
33. S. Eu *et al.*, *J. Phys. Chem. C* **111**, 3528 (2007).
34. T. Bessho, S. M. Zakeeruddin, C. Y. Yeh, E. W. G. Diau, M. Grätzel, *Angew. Chem. Int. Ed.* **49**, 6646 (2010).
35. H.-P. Lu *et al.*, *J. Phys. Chem. C* **113**, 20990 (2009).
36. C.-P. Hsieh *et al.*, *J. Mater. Chem.* **20**, 1127 (2010).
37. S.-L. Wu *et al.*, *Environ. Sci.* **3**, 949 (2010).
38. J.-C. Chang, C.-J. Ma, G.-H. Lee, S.-M. Peng, C.-Y. Yeh, *Dalton Trans.* **8**, 1504 (2005).
39. H.-P. Lu *et al.*, *Phys. Chem. Chem. Phys.* **11**, 10270 (2009).
40. C.-L. Mai *et al.*, *Chem. Commun. (Camb.)* **46**, 809 (2010).
41. H. J. Snaith *et al.*, *Nanotechnology* **19**, 424003 (2008).
42. B. C. O'Regan, F. J. Lenzmann, *J. Phys. Chem. B* **108**, 4342 (2004).
43. B. C. O'Regan, Bakker, J. Kroeze, H. Smit, P. Sommeling, James R. Durrant, *J. Phys. Chem. B* **110**, 17155 (2006).
44. P. Siders, R. A. Marcus, *J. Am. Chem. Soc.* **103**, 741 (1981).
45. J. N. Clifford, E. Martínez-Ferrero, A. Viterisi, E. Palomares, *Chem. Soc. Rev.* **40**, 1635 (2011).
46. J. J. Nelson, T. J. Amick, C. M. Elliott, *J. Phys. Chem. C* **112**, 18255 (2008).

Acknowledgments: E.W.-G.D. and C.Y.Y. acknowledge the financial support from the National Science Council of Taiwan and Ministry of Education of Taiwan. M.G. thanks the European Research Council (ERC) for an Advanced Research Grant (ARG 247404) funded under the "Mesolight" project. Financial support under the European community's 7th FWP for project 227057 (INNOVASOL) and under a grant from the Dayton U.S. Air force Research Laboratory is gratefully acknowledged.

M.K.N. thanks World Class University program, Photovoltaic Materials, Department of Material Chemistry, Korea University, Chungnam 339-700, Korea, which is funded by the Ministry of Education, Science and Technology through the National Research Foundation of Korea (R31-2008-000-10035-0). We thank R. Humphry-Baker for fruitful discussions as well as optical measurements and M. J. M. Bonnet-Eymard from the IMT Photovoltaic Laboratory for assistance with the cell photovoltaic performance measurements.

Supporting Online Material
www.sciencemag.org/cgi/content/full/334/6056/629/DC1
Materials and Methods
Figs. S1 to S12
Tables S1 to S4
References (*47*, *48*)

13 June 2011; accepted 23 September 2011
10.1126/science.1209688

REPORTS

Structural Dynamics of a Catalytic Monolayer Probed by Ultrafast 2D IR Vibrational Echoes

Daniel E. Rosenfeld,* Zsolt Gengeliczki,* Brian J. Smith, T. D. P. Stack, M. D. Fayer†

Ultrafast two-dimensional infrared (2D IR) vibrational echo spectroscopy has proven broadly useful for studying molecular dynamics in solutions. Here, we extend the technique to probing the interfacial dynamics and structure of a silica surface-tethered transition metal carbonyl complex—tricarbonyl (1,10-phenanthroline)rhenium chloride—of interest as a photoreduction catalyst. We interpret the data using a theoretical framework devised to separate the roles of structural evolution and excitation transfer in inducing spectral diffusion. The structural dynamics, as reported on by a carbonyl stretch vibration of the surface-bound complex, have a characteristic time of ~150 picoseconds in the absence of solvent, decrease in duration by a factor of three upon addition of chloroform, and decrease another order of magnitude for the bulk solution. Conversely, solvent-complex interactions increase the lifetime of the probed vibration by 160% when solvent is applied to the monolayer.

Tailoring surface properties by depositing molecular monolayers (*1*) on various solid substrates is critical to many technologies, including industrial catalysis, chemical sensors (*2*), fuel cells, and molecular electronics (*3*). The functional groups terminating the monolayer determine the hydrophobicity, chemical reactivity (*4*), and charge transfer properties (*5*) of the interface, which are strongly influenced by local structure and fast associated dynamics. Despite a long-standing need, the tools to study structural dynamics of interfacial molecules under chemically relevant conditions have been lacking (*6*). Commonly used microscopy and scattering techniques provide information on the size, shape, and electronic structure of particles and adsorbates, but their time resolution is generally insufficient to study molecular dynamics, and many only function under ultrahigh vacuum conditions (*7*).

The development of ultrafast infrared (IR) spectroscopy over the past two decades has provided tools for the in-depth examination of the dynamics and structure of bulk liquids, liquids in nanoscopic environments, organic complexes, biological macromolecules, and solids (*8*–*11*). IR techniques such as pump-probe absorption, transient grating, and two-dimensional (2D) IR vibrational echo spectroscopy have been used to study spectral diffusion (*9*), vibrational relaxation (*12*), chemical exchange, (*8*, *10*), and orientational dynamics (*11*). The extension of these techniques to surfaces and interfaces has been a long-standing goal of the surface and ultrafast spectroscopy communities (*13*).

Sum-frequency generation (SFG) and second-harmonic generation (SHG) form the current basis for vibrational spectroscopy of surfaces and interfaces. Frequency-domain experiments provide important information on the molecular orientation (*14*), vibrational coupling (*15*), and hydrogen-bond network at interfaces (*16*), whereas time-domain studies can probe reorientational (*17*) and translational motions (*18*), thermal conductance (*19*), vibrational relaxation (*20*), and spectroscopic line broadening (*21*). The measurement and quantitative interpretation of 2D IR spectra of molecular adsorbates has previously been limited to thick samples and attempts at 2D IR-pump SFG-probe spectroscopy (upconverted hole-burning) (*22*, *23*). Upconverted two-pulse vibrational echoes, which measure the homogeneous component (ultrafast motionally narrowed dynamics) of the infrared absorption spectrum but cannot study spectral diffusion (time dependence of structural evolution), have been attempted as well (*21*, *24*). The frequency upconversion in time-resolved SFG renders interpretation difficult because of the included Raman process (*23*), which necessitates careful determination of the time correlation functions measured in the given beam geometry (*25*). Furthermore, SFG-based techniques are inherently insensitive because upconversion is inefficient. Techniques relying on hole-burning methods have intrinsically lower time resolution and sensitivity and produce convoluted spectra, whereas echo-based methods suffer none of these drawbacks (*26*).

Here, we report on the application of an ultrafast 2D IR vibrational echo method to molecular monolayers that overcomes all of these challenges, because there is no intrinsic tradeoff between time and frequency resolution, and the associated heterodyne detection provides much higher sensitivity (signal-to-noise ratio) than other methods. This approach opens the way for the quantitative understanding of the effect of immobilization and solvent on the structural and vibrational dynamics of molecular monolayers on solid substrates.

We applied our technique to the study of a silica-immobilized transition metal carbonyl compound of interest as a photocatalyst. Immobilized homogeneous catalysts are appealing because they maintain high molecular specificity and activity under mild conditions while precluding the need for expensive separation methods (*27*–*29*). However, conditions such as the presence or absence of solvent can strongly affect catalytic activity in presently unpredictable ways (*29*, *30*). Microscopic changes affecting molecular reactivity should manifest themselves in the dynamical characteristics of the system due to the small energy differences among states. As a first step toward resolving solvent-dependent vibrational dynamics that could ultimately assist rational catalyst optimization, we have compared spectral diffusion rates and vibrational lifetimes of bare (monolayer/air interface) versus solvated surface-bound complexes. In addition, the dynamics of the immobilized catalyst are compared to the corresponding homogeneous catalyst in bulk solution.

We immobilized a compound in the $LRe(CO)_3X$ class of complexes (L, heteroaromatic bidentate ligand; X, halide/pseudohalide) that are under investigation as homogeneous photo/electro-catalysts for the reduction of CO_2 to CO or formate (*30*). Other metal-ligand–based catalysts have been immobilized (*27*), and the system depicted in Fig. 1 represents a good model system for studying

Department of Chemistry, Stanford University, Stanford, CA 94305, USA.

*These authors contributed equally to this work.
†To whom correspondence should be addressed. E-mail: fayer@stanford.edu